Environmental Science Nano

ROYAL SOCIETY OF CHEMISTRY

PAPER

View Article Online
View Journal | View Issue

Cite this: *Environ. Sci.: Nano*, 2024, 11, 4186

Nanoarchitectonics with $W_{18}O_{49}$ nanobelts and B-doped g-C_3N_4 nanosheets towards NO and 4-nitrophenol conversion

Xiao Zhang, *[a] Xiang Xia[b] and Ping Yang *[b]

Received 6th May 2024,
Accepted 22nd July 2024

DOI: 10.1039/d4en00399c

rsc.li/es-nano

Construction of heterostructures has been an effective approach for suppressing recombination of photogenerated charge carriers of graphitic carbon nitride (g-C_3N_4) materials and facilitating solar energy harvesting. In this paper, superior thin B-doped g-C_3N_4 nanosheets are synthesized *via* mechano-chemical pre-treatment and two-step thermal polymerization (at 600 and 700 °C) using boric acid and melamine as precursors. The *in situ* growth of $W_{18}O_{49}$ nanobelts on B-g-C_3N_4 nanosheets is attained *via* solvothermal synthesis. $W_{18}O_{49}$ nanobelts are horizontally implanted onto g-C_3N_4 nanosheets to construct a Z-scheme heterostructure with extended light absorption in the near infrared range. Well-developed interfaces between $W_{18}O_{49}$ and B-g-C_3N_4 are crucial for the enhanced transfer efficiency of photogenerated charge carriers. The $W_{18}O_{49}$/B-g-C_3N_4 samples fabricated using optimized conditions show excellent photocatalytic performance in NO and 4-nitrophenol oxidation conversion. The $W_{18}O_{49}$/B-g-C_3N_4 composites attain a NO removal efficiency of 64% (at an initial NO concentration of 600 ppb in air) with a low NO_2 selectivity (6.4%), which is more efficient than that of the commercial P25 (TiO_2, with a 40% NO removal rate). These are mainly attributed to the formed Z-scheme $W_{18}O_{49}$/B-g-C_3N_4 layered heterostructure, increased specific surface area and improved interfacial structure. The heterostructure construction, light absorption range extension, and adjustment on the band gap of the composite material are discussed in detail. Under full-spectrum irradiation conditions, the $W_{18}O_{49}$/B-g-C_3N_4 heterostructures also show excellent light-assisted 4-nitrophenol elimination (*via* selective hydrogenation to valuable 4-aminophenol) performance, attaining a 99% 4-nitrophenol reduction rate.

Environmental significance

Large amounts of pollutants were produced in thermal power and industrial and transportation processes. A clean and efficient method is urgently needed to remove nitrogen oxides. Photocatalysis oxidation as an efficient approach can remove nitrogen oxides and 4-nitrophenol. Heterostructure formation, significantly suppressed charge carrier recombination, and enhanced solar light harvesting ability were the key factors that lead to the much-improved photocatalytic activity of $W_{18}O_{49}$/B-g-C_3N_4 heterostructure catalysts. The horizontal implantation of $W_{18}O_{49}$ nanobelts on B-g-C_3N_4 was one of the keys for the formation of the $W_{18}O_{49}$/B-g-C_3N_4 Z-scheme heterostructure with extended light absorption (to the near infrared region) and improved interfacial structures. The 64% NO removal (higher than that of the commercial P25, with a quite low selectivity to NO_2 of 6.4%) and the 99% 4-NP reduction rate (to 4-aminophenol, under full-spectrum condition) observed for the $W_{18}O_{49}$/B-g-C_3N_4 composites prepared using optimized parameters could be ascribed to the attained formation of the Z-scheme layered heterostructures possessing adjusted band structures, increased surface active sites and well-developed interfaces.

Introduction

Environmental pollution and climate change are a growing threat to human health.[1–3] Nitrogen oxides (NO_x), as one common air pollutant (that are formed due to fuel combustion processes and often contribute to photochemical smog/acid rain formation) with high toxicity, have been one of the leading causes of deadliest chronic diseases (*e.g.*, cancer).[4–6] It is generally accepted that NO (as one principal nitrogen oxide species) has been considered difficult to remove directly, thus it is often oxidized/reduced into other relatively easy-to-manage intermediate species.[7,8] Conventional pre-treated NO emission elimination methods include various pre-treatments that could be conducted on fuels prior to use; however, the relatively low efficiency and

[a] *Faculty of Chemical Engineering and Technology, Cracow University of Technology, Krakow, Poland. E-mail: friends_zhangxiao@yahoo.co.jp*
[b] *School of Materials Science and Engineering, University of Jinan, Jinan, 250022, PR China. E-mail: mse_yangp@ujn.edu.cn*

large workload often restricted their application.[9] In contrast, exploitation of photocatalytic techniques provides the possibility of attaining NO removal *via* a much greener, low-cost, and high-efficiency route.[10] For instance, TiO_2 as a typical photocatalyst reported in the literature has been demonstrated to adsorb H_2O and O_2 molecules, generating reactive species that can oxidize NO species under ultraviolet (UV) light irradiation conditions.[11] However, one major issue encountered in this case is that the efficiency and solar energy harvesting ability of TiO_2 are often not that satisfactory. It is therefore important to explore novel photocatalysts with an extended light absorption range and high NO removal efficiency, as well as high value-added product/intermediate conversion rate (*e.g.*, reduction of 4-nitrophenol (4-NP) to 4-aminophenol).[12]

As a widely exploited metal-free visible-light-responsive photocatalyst, graphitic carbon nitride (g-C_3N_4, built from triazine and tri-*s*-triazine rings) has been extensively investigated in a variety of catalytic energy conversion and fuel production related applications (*e.g.*, water splitting, CO_2 conversion, *etc.*).[13–18] Exploitation of g-C_3N_4 based photocatalysts in NO removal and NH_3 generation have been two appealing topics in the recent decade.[17] In order to extend light absorption and to suppress the relatively high charge recombination of bulk g-C_3N_4 (having a band gap of 2.7 eV and a relatively low surface area of around 20 $m^2\ g^{-1}$), investigations have been focused on the synthesis of thin 2D g-C_3N_4 nanosheets and the construction of g-C_3N_4 based composite materials with adjusted band structure as well as enhanced performance.[19] Since the band gap of g-C_3N_4 is often directly related to the thickness, morphology, and crystallinity of the material, adjusted microstructures of ultrathin 2D g-C_3N_4 based heterostructures could be attained by combining g-C_3N_4 with metals or semiconducting nanocomponents, constructing heterostructures with improved stability and desirable morphology. These g-C_3N_4 based heterostructure composites with a tunable band gap and high stability as well as excellent efficiency have been promising catalyst materials that can be utilized for a variety of photocatalytic energy conversion and pollutant treatment applications (involving NO and 4-NP conversion).[15,20–22]

Solar energy harvesting ability has been another important factor that determines the performance of a photocatalyst. Constructing g-C_3N_4 based composites with extended light absorption, enhanced redox ability, and high catalytic activity is thus important. By loading another semiconductor decorated nanocomposite (*e.g.*, tungsten oxides involving $W_{18}O_{49}$, WO_3, and WO_2, having a tunable band gap of around 2–3 eV) onto g-C_3N_4, extension of the light absorption range of the composite material could be attained (*e.g.*, from visible (vis) to near infrared (NIR) and full-spectrum range).[22,23] In the case of 2D tungsten oxide nanocomponent decoration, the presence of abundant oxygen vacancies, the localized surface plasmon resonance (LSPR) effect of tungsten oxides, and the formation of 2D/2D layered heterostructures (using a g-C_3N_4 nanosheet base) are pivotal to improving the catalytic activity of the composite material.[24,25] Examples of 2D tungsten oxide modified carbon based composite photocatalysts that have been reported for photocatalytic degradation under full-spectrum conditions include a $W_{18}O_{49}$ nanobelt incorporated Z-scheme rGO/TiO_2-bronze/$W_{18}O_{49}$ ternary heterostructure and an *in situ* grown WO_x nanoplate modified g-C_3N_4 based Z-scheme heterostructure.[26,27] In this case, attaining control of the growth of 2D tungsten oxide components (*e.g.*, nanobelts) in the g-C_3N_4 nanosheet based system can be important for constructing satisfactory 2D/2D heterostructures. The growth kinetics of decorated nanocomponents and the catalytic performance of the composite system are governed by the composition, the thickness, and the crystallinity of the g-C_3N_4 base.

Elemental doping and additional nanocomponent decoration were the keys to the tuned band gap/composition and the attained enhanced catalytic performance of the composite catalysts in this paper.[28–30] Ultrathin B-doped g-C_3N_4 nanosheets with increased surface active sites were fabricated using a two-step thermal polymerization method as reported in our previous work, and a solvothermal synthesis (at 180 °C) method was used to decorate $W_{18}O_{49}$ nanobelts on the superior thin B-doped g-C_3N_4 nanosheet base. The formed layered 2D/2D $W_{18}O_{49}$/B-g-C_3N_4 Z-scheme heterostructures with a narrow band gap showed expanded light response to the NIR region. The heterostructure photocatalyst fabricated using optimized parameters was able to remove 64% of NO (at an initial NO concentration of 600 ppb in air, with a reasonably low NO_2 selectivity of 6.4%) and a 99% 4-NP conversion efficiency under full-spectrum conditions.

Experimental section

Chemicals

Melamine, WCl_6, boric acid (H_3BO_3), ascorbic acid (AA), rhodamine (RhB), ethylene glycol, and *tert*-butanol were supplied by Merck Ltd. Other chemicals such as ethanol, 4-NP, isopropanol (IPA), potassium biphthalate ($C_8H_5KO_4$), triethanolamine (TEOA), ethylenediaminetetraacetic acid disodium salt (EDTA-2Na), potassium iodide (KI), *p*-benzoquinone (*p*-BQ), nitroblue tetrazolium (NBT), chloroplatinic acid hexahydrate (H_2PtCl_6), and sodium sulfate were purchased from Sinopharm Chemical Reagent Co. Ltd. All chemicals were directly used with no further purification. Commercial TiO_2 (P25, 99.9%) containing 80% anatase and 20% rutile was purchased from Evonik Industries AG.

Preparation of samples

The B-doped g-C_3N_4 nanosheet (denoted as BCN) base was synthesized using a mechano-chemical pre-reaction and two-step thermal polymerization (at 600 and 700 °C) combined treatment method. H_3BO_3 was mixed with melamine at a weight percentage of 5 wt%. The powder mixture was ground to undergo the mechano-chemical treatment process before calcination at 600 °C for 1 hour (using a ramp rate of 5 °C

min^{-1}, in N_2) to obtain the bulk B-doped g-C_3N_4 product. The ultrathin B-doped g-C_3N_4 nanosheet sample was then fabricated through conducting further thermal polymerization treatment on this bulk B-g-C_3N_4 sample for 1 hour at 700 °C using a much slower ramp rate of 2 °C min^{-1}, followed by washing with deionized water/ethanol several times and drying.

Solvothermal synthesis was applied for implanting $W_{18}O_{49}$ nanobelt components onto B-doped g-C_3N_4 nanosheets with ethylene glycol used as the solvent. The precursors WCl_6 and AA were mixed in ethylene glycol at a molar ratio of 1 : 10 to obtain a mixture solution. A certain amount of the prepared thin B-doped g-C_3N_4 nanosheet (BCN) sample was then added into this solution with vigorous stirring followed by 5 min of sonication treatment. The obtained suspension was then poured into a Teflon-lined autoclave to undergo 10 hours of solvothermal treatment at 180 °C, before washing and drying to obtain the final $W_{18}O_{49}$/B-g-C_3N_4 composite sample. The composite samples prepared using the WCl_6 to BCN weight percentage of 25, 30, and 35 wt% were denoted as samples $W_{18}O_{49}$/BCN-1, $W_{18}O_{49}$/BCN-2, and $W_{18}O_{49}$/BCN-3, respectively.

Characterization

The transition electronic microscopy (TEM) data of the heterostructure sample were collected on a Tecan F200 (FEI). A Kratos Axis Ultra DLD spectrometer was used for X-ray photoelectron spectroscopy (XPS) analysis with monochromatic AlKα (1486.6 eV) X-rays operated at 150 W, and a Bruker D8 X-ray diffractometer with a Cu Kα radiation source was used for recording X-ray diffraction (XRD) patterns of the samples. The UV-vis diffuse reflectance spectra (DRS) data and the Fourier transform infrared (FTIR) spectra of the samples were recorded using a Hitachi U-4100 UV-vis spectrophotometer and Nicolet 380 FTIR spectrometer (Thermo Fisher Scientific). An ASIQC0000-4 analyser (Quantachrome Instrument) was used to collect the N_2 adsorption–desorption isotherm curve data for surface area and pore structure analysis using the Brunauer–Emmett–Teller (BET) method, and the photoluminescence spectra of the samples were collected on a Hitachi F-4600 fluorescence spectrophotometer. In addition, a CHI660E electrochemical workstation was used to record the Mott–Schottky plots of the samples for band position analysis, and a Bruker A300 electron spin resonance (ESR) spectrometer was required for free radical analysis.

Photocatalytic of NO removal

The photocatalytic NO oxidation test at room temperature was carried out using a reaction chamber, compressed NO gas cylinder, and NO_x analyser (Thermo Fisher Scientific) combined testing system. The 500 ppm NO concentration in air was diluted to 600 ppb which was passed into the reactor. A 200 W xenon lamp was used to simulate sunlight and placed above the reactor. During the experiment, circulating water was used to maintain the reaction temperature at room temperature. NO gas bubbling (0.5 hour) treatment was necessary for the sample (100 mg, on a quartz glass sheet that was anchored on the bottom plate of the reactor) before conducting the NO oxidation measurements under full spectrum conditions (using a 300 W Xe lamp light source). The equation $(1 - C/C_0) \times 100\%$ (with C_0 referring to the initial NO concentration) was utilized for determining the NO removal efficiency of the samples. In the case of NO oxidation cycling stability test, the measurements were carried out with the light source switched off at the end of each 10 minute testing cycle.

Photo-assisted 4-NP removal.

10 mg of the catalyst sample was mixed with 50 mL of aqueous solution containing 0.1 mM 4-NP and 1 mM $NaBH_4$. 2 mL of the sample solution was then taken from the testing system (having a 300 W xenon lamp as the light source) at 3 min time interval (with a 0.22 μm membrane used as the filter). The Hitachi U-4100 UV-vis spectrophotometer was used for collecting the absorbance data of the sample solution. For active species determination measurements under full-spectrum conditions, a similar procedure was applied except for the trapping agent addition part. In this case, $K_2Cr_2O_7$, EDTA-2Na, IPA and *p*-benzoquinone were utilized to trap the photoinduced e^-, holes, ·OH and $\cdot O^{2-}$ radical species, respectively.

Results and discussion

For the fabrication of B-doped ultrathin g-C_3N_4 nanosheets, the multi-step thermal polymerization process (at quite high temperature using a relatively low heating rate) and the mechano-chemical pre-treatment were pivotal to the homogeneous doping of B elements in the g-C_3N_4 network.[31,32] Scheme 1 shows the formation process of $W_{18}O_{49}$-B-g-C_3N_4 composites. The mechano-chemical pre-treatment and the adsorption of W^{6+} ions played the key role in homogeneous growth of $W_{18}O_{49}$ nanobelts. The optimized parameter for B precursor incorporation in this case was 5 wt%, attaining the fabrication of a BCN base with satisfactory photocatalytic activity. The quite slow thermal polymerization

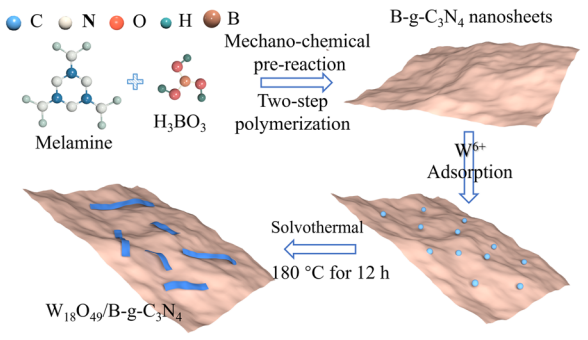

Scheme 1 Synthesis illustration of $W_{18}O_{49}$-B-g-C_3N_4 composites.

process and the high temperature setting used during thermal polymerization were the keys to the formation of superior thin nanosheets. The B component was successfully incorporated into the C and N rich triazine (C_3N_3) and tri-*s*-triazine (heptazine, C_6N_7) building blocks of g-C_3N_4. During the $W_{18}O_{49}$ nanobelt solvothermal growth process, the addition of ascorbic acid was pivotal to the generation of oxygen vacancies in the composite system. By adjusting the ratios of WCl_6 to the BCN base, 2D/2D $W_{18}O_{49}$/B-g-C_3N_4 layered heterostructure composites ($W_{18}O_{49}$/BCN samples) with optimized parameters and performance were constructed. The TEM images of the composites are shown in Fig. 1, with the images of two selected areas of the horizontally grown $W_{18}O_{49}$ nanobelt modified B-g-C_3N_4 nanosheets (sample $W_{18}O_{49}$/BCN-2) at relatively low magnification shown in Fig. 1a and b. As observed in Fig. 1c, the nanobelts were completely embedded into the B-g-C_3N_4 base network in bended, linear, or overlapped forms with no clear interfaces observed between the B-g-C_3N_4 base and the decorated $W_{18}O_{49}$ nanocomponents. Due to the presence of more abundant surface and structural defects on the B-doped g-C_3N_4 nanosheet base (compared with those on pristine g-C_3N_4), $W_{18}O_{49}$ nanobelts with broad size distribution were observed (as shown in Fig. 1d). These defects acted as the growth active sites for monomer deposition and $W_{18}O_{49}$ nucleation, resulting in closely implanted nanobelt components on the nanosheet base. The lattice fringes with a spacing of 0.37 nm in Fig. 1e corresponded to the (010) facet of $W_{18}O_{49}$, and the 0.32 nm lattice spacing in Fig. 1f (observed on the B doped g-C_3N_4 nanosheets with quite clear lattice fringes) was attributed to the (002) facet of g-C_3N_4.[33]

XPS analysis was also performed on the samples and the results are shown in Fig. 2. Fig. 2a shows the survey spectra of samples $W_{18}O_{49}$, BCN, and $W_{18}O_{49}$/BCN-2. Clear C 1s and N 1s peaks were observed for the B-doped g-C_3N_4 base (sample BCN); characteristic W 4f and O 1s peaks were observed for the $W_{18}O_{49}$ sample; while a survey spectrum with C, N, O, W, and B peaks was recorded for sample $W_{18}O_{49}$/BCN-2. The high-resolution C 1s spectrum of sample BCN in Fig. 2b could be fitted into three peaks that were assigned to C–C (sp^2 hybridized carbon, at 284.80 eV), C–N/C═O (carbonyl group, at 288.15 eV), and C–OH (epoxy/hydroxyl group, 286.41 eV). Compared to BCN, a shift towards a higher energy level was observed for the C–OH and C–N/C═O peaks after $W_{18}O_{49}$ incorporation, because of the interactions between the $W_{18}O_{49}$ and B-g-C_3N_4 components as well as the changes in structure (of the nanosheet base) resulting from solvothermal treatment. Three characteristic peaks involving C–N═C (pyridinic-N, 398.79 eV), N–$(C)_3$

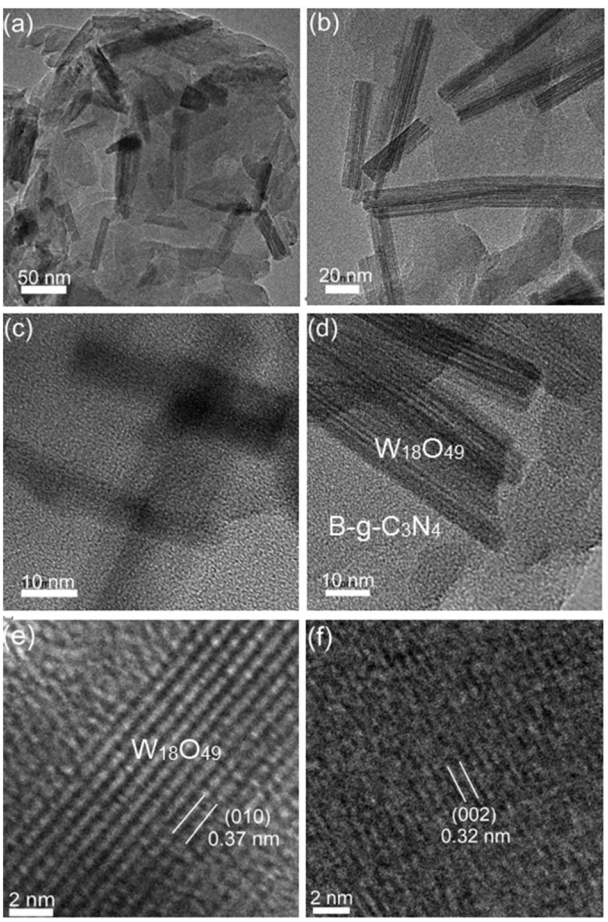

Fig. 1 TEM images of the composite sample $W_{18}O_{49}$/BCN-2: (a and b) images at lower magnification, (c and d) selected areas of the $W_{18}O_{49}$ nanobelts implanted onto g-C_3N_4 nanosheets, (e) enlarged lattice fringes of the $W_{18}O_{49}$ nanobelts, and (f) enlarged area of the lattice fringes of the g-C_3N_4 nanosheets. $W_{18}O_{49}$ phase was indicated in (c) and (d), in which it covered the B-g-C_3N_4 nanosheets.

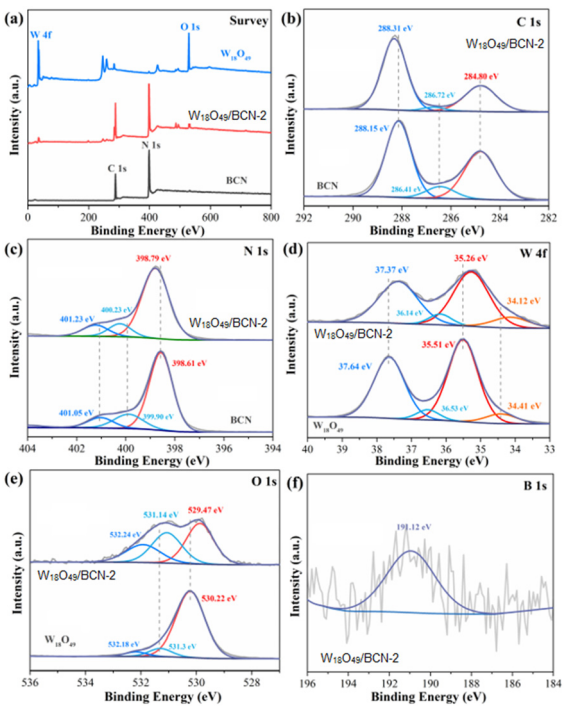

Fig. 2 XPS spectra obtained for samples $W_{18}O_{49}$, BCN, and $W_{18}O_{49}$/BCN-2: (a) survey spectra, (b) C 1s spectra, (c) N 1s spectra, (d) W 4f spectra, (e) O 1s spectra, and (f) B 1s spectra.

(pyrrolic-N, 400.23 eV), and N–H (graphitic N, 401.23 eV) peaks were observed in the N 1s spectrum of sample $W_{18}O_{49}$/BCN-2 (Fig. 2c).[34] A shift towards higher binding energy was observed for all the N characteristic peaks of the sample after $W_{18}O_{49}$ modification (sample $W_{18}O_{49}$/BCN-2). In contrast, a shift towards a lower energy level was observed for the W 4f spectrum of the composite sample $W_{18}O_{49}$/BCN-2 in comparison with its pure $W_{18}O_{49}$ counterpart (as shown in Fig. 2d). The peaks positioned at 35.26 and 36.34 eV in Fig. 2d were assigned to the W $4f_{7/2}$ and W $4f_{5/2}$ peaks of the W^{6+} state, respectively, whereas the peaks corresponding to the W^{5+} state were located at 34.12 and 37.37 eV.[35] In comparison with the pure $W_{18}O_{49}$ sample, red-shifted O 1s peaks (towards lower binding energy) were observed for the $W_{18}O_{49}$/BCN-2 composite sample (Fig. 1e), confirming the successful incorporation of $W_{18}O_{49}$ components on B-g-C_3N_4. The three peaks (observed in the high-resolution O 1s spectrum of $W_{18}O_{49}$/BCN-2 in Fig. 2e) positioned at 529.47, 531.14, and 532.24 eV corresponded to the oxides, hydroxides, and water/organics species in the composite system.[36] The peaks of the O 1s spectrum observed for $W_{18}O_{49}$ incorporated B-g-C_3N_4 was different from that of pure $W_{18}O_{49}$, confirming the interaction between $W_{18}O_{49}$ and B-g-C_3N_4. In this case, the interaction between the tungsten oxide components and the B-doped g-C_3N_4 base was confirmed by the presence of oxides that came from the $W_{18}O_{49}$ lattice oxygen and the chemisorbed oxygen species, as well as the quite large differences in peak intensity and position observed for the composite sample compared with its pure $W_{18}O_{49}$ counterpart.[22] The weak B 1s peak signal in Fig. 1f confirmed that the doped amount of the B component in the composite system was quite low, and this was attributed to the limited tendency of B incorporation in g-C_3N_4 nanosheets due to the potential differences in microstructures of the two components.

N_2 adsorption and desorption isotherm curves of samples BCN and $W_{18}O_{49}$/BCN-2 (Fig. 3) were collected to investigate the BET specific surface area of the samples. An increased surface area from 81.91 to 132.63 $m^2\ g^{-1}$ was observed for the $W_{18}O_{49}$ immobilized composite sample ($W_{18}O_{49}$/BCN-2). The increased specific surface area of the composite system was pivotal to increasing the active sites and enhancing the solar harvesting ability and target molecule adsorption capacity, therefore improving the photocatalytic activity of the material.

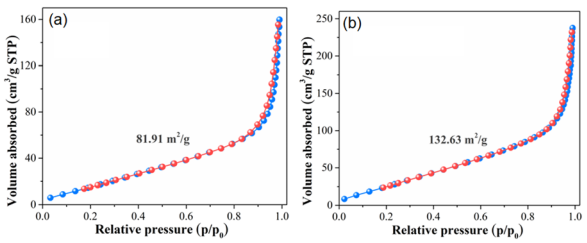

Fig. 3 Nitrogen adsorption–desorption isotherm curves of (a) sample BCN and (b) sample $W_{18}O_{49}$/BCN-2.

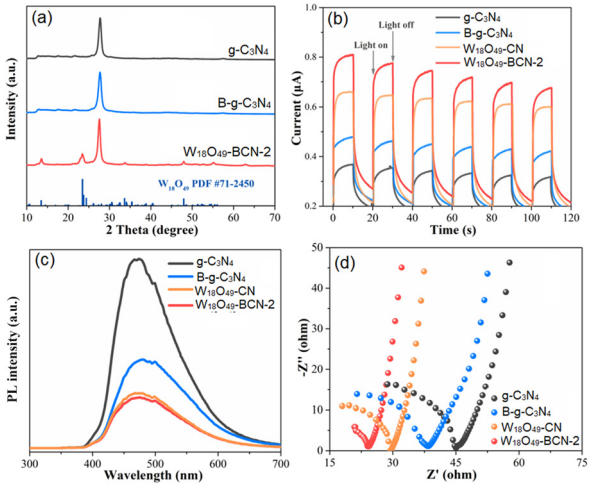

Fig. 4 (a) XRD patterns collected for the samples, (b) transient photocurrent response plots, (c) photoluminescence spectra, and (d) electrochemical impedance spectroscopy plots collected for pure g-C_3N_4 and composite samples.

The XRD patterns of pristine g-C_3N_4 and the composite samples were collected, and the results are shown in Fig. 4a. The two peaks located at 13.0 and 27.8° were attributed to the (100) and (002) facets of the g-C_3N_4 phase of samples g-C_3N_4, BCN, and $W_{18}O_{49}$/BCN-2. In addition to the g-C_3N_4 related diffraction peaks, clear monoclinic phase $W_{18}O_{49}$ (JCPDS no. 71-6450) characteristic peaks were observed on sample $W_{18}O_{49}$/BCN-2, confirming the successful immobilization of $W_{18}O_{49}$ components on B-g-C_3N_4. The transient photocurrent response results in Fig. 4b demonstrated that the B-doped g-C_3N_4 composites had enhanced transient photocurrent response compared with that of pristine g-C_3N_4 because of the improved transport efficiency of photogenerated charges due to B doping. Moreover, a much-improved transient photocurrent response rate was observed for the $W_{18}O_{49}$ nanobelt incorporated composite sample $W_{18}O_{49}$/BCN-2, suggesting the further facilitated charge carrier transport after $W_{18}O_{49}$ incorporation. In order to further investigate the role of $W_{18}O_{49}$ in the composite system, a comparison composite sample having $W_{18}O_{49}$ nanobelts immobilized onto the pristine g-C_3N_4 nanosheets (sample $W_{18}O_{49}$-CN in Fig. 4) was prepared using a similar methodology, and an enhanced transient photocurrent response rate (that was higher than that of the B-g-C_3N_4 and g-C_3N_4 samples) was observed. The photoluminescence spectra data were also collected for the samples (Fig. 4c). In general, a decrease in photoluminescence intensity is often accompanied with an increase in photogenerated charge carrier separation efficiency, and this further confirmed that the $W_{18}O_{49}$/BCN-2 composites have significantly suppressed charge recombination compared with that of other samples. In addition, since it is generally accepted that the smaller the arc radius, the lower the charge transfer resistance, the electrochemical impedance spectra (EIS) results in Fig. 4d

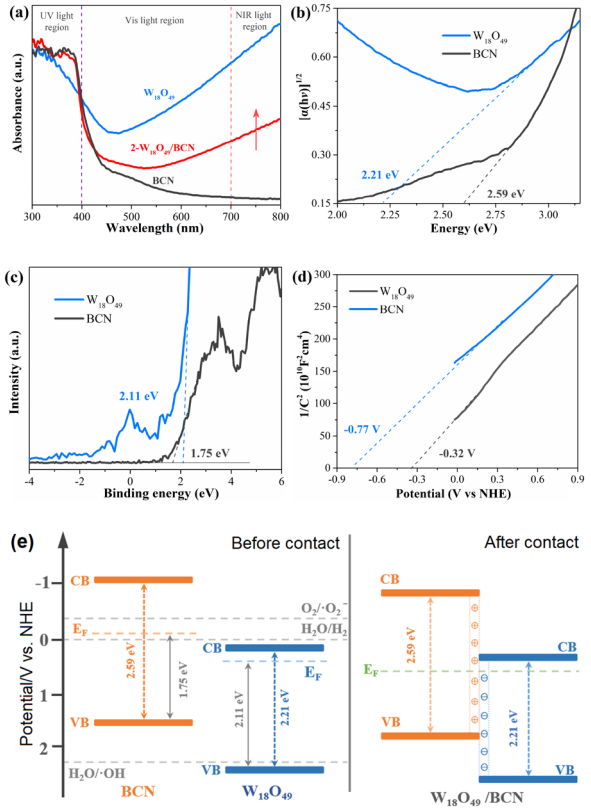

Fig. 5 (a) UV-vis diffuse reflectance spectra of samples $W_{18}O_{49}$, BCN, and $W_{18}O_{49}$/BCN-2. (b) Tauc plots obtained based on (a). (c) XPS valence band spectra of the samples. (d) Mott–Schottky plots obtained for the samples. (e) Illustration of the proposed band structure of the composites before and after heterostructure formation.

also indicated that sample $W_{18}O_{49}$/BCN-2 showed the lowest charge transfer resistance among all the samples.

UV-vis diffuse reflectance spectra, XPS valence band spectra and Mott–Schottky plots of the samples (Fig. 5) were collected for investigating the band positions/structures and charge transport mechanisms of the $W_{18}O_{49}$/B-g-C_3N_4 composite system. The UV-vis diffuse reflectance spectra in Fig. 5a showed that after $W_{18}O_{49}$ immobilization, the absorption of the composite samples in both vis and NIR regions was significantly extended. In this case, the significantly enhanced light absorption and the constructed unique 2D/2D surface-to-surface structure of the $W_{18}O_{49}$ immobilized B-g-C_3N_4 composites were the keys to the increased number of exposed active sites, improved energy harvesting ability and enhanced photocatalytic activity of the material. The Tauc plots obtained based on the UV-vis diffuse reflectance spectra using the transformed Kubelka–Munk equation below are shown in Fig. 5b.[27,32]

$$\alpha h\upsilon - A(h\upsilon - E_g)^n$$

where n = 0.5 in the case of the indirect band gap semiconductor, n = 2 in the direct band gap semiconductor case; E_g, α, h, A, and υ correspond to the band gap, absorption coefficient, Planck constant, proportionality constant, and light frequency, respectively.[27] The estimated band gap (E_g value) of BCN and $W_{18}O_{49}$ were 2.59, and 2.21 eV (respectively), while the XPS valence band (VB) spectra of the two samples BCN and $W_{18}O_{49}$ (in Fig. 5c) showed a 0.36 eV difference in VB edge positions. The more positive VB position of the B-doped g-C_3N_4 components was crucial for attaining enhanced oxidation ability of the material.

Fig. 5d shows the Mott–Schottky plots recorded for samples BCN and $W_{18}O_{49}$. The flat band potentials calculated for samples BCN and $W_{18}O_{49}$ were −0.77 and −0.32 V (respectively). With the potential referring to the normal hydrogen electrode (NHE), the conduction band (CB) and VB positions of samples BCN and $W_{18}O_{49}$ were estimated utilizing the equation shown below, and the schematic illustration of the band structures of the composite system containing the BCN and $W_{18}O_{49}$ components is shown in Fig. 5e.

$$E_{(NHE)} = E_{(Ag/AgCl)} + 0.0591 \times pH + 0.197$$

Once the $W_{18}O_{49}$ nanobelts were decorated onto the B-doped g-C_3N_4 nanosheet base forming the heterostructure system, a decrease in the Femi level of the $W_{18}O_{49}$/B-g-C_3N_4 composites was observed, owing to the higher work function of the $W_{18}O_{49}$ components in comparison with that of the B-g-C_3N_4 components. Since the transfer of photoinduced electrons are often observed from the surface of the B-g-C_3N_4 components to the $W_{18}O_{49}$ part until attaining aligned Fermi levels, the accumulation of photoinduced charges at the composite interfaces could lead to the formation of a built-in electric field and upward bent band at the interfaces, forming Z-scheme $W_{18}O_{49}$/B-g-C_3N_4 heterostructures with abundant oxygen vacancies and enhanced localized surface plasmon resonance (LSPR) absorption (owing to the presence of $W_{18}O_{49}$ in the composite system).[25] In addition, the assorted charge transfer path of the nonstoichiometric $W_{18}O_{49}$ components (involving photoinduced electron transfer from the VB to CB, charge transition between the VB and the oxygen vacancy associated energy states, and LSPR excitation induced charge transfer) was also one of the keys for the much-enhanced charge transfer efficiency and catalytic activity observed for the $W_{18}O_{49}$/B-g-C_3N_4 composites.

Investigation on the photocatalytic NO removal performance of the composite samples was performed and the results are shown in Fig. 6a. With the pristine g-C_3N_4 nanosheet sample showing a quite low NO removal rate of 28%, the B doped sample (BCN) showed a much-improved removal rate of 50%, demonstrating that B doping was beneficial for enhancing the light absorption, increasing the number of active sites for NO adsorption and narrowing the band gap for enhancing the redox ability of the material.

The poor NO removal performance observed for the pure $W_{18}O_{49}$ sample indicated the limited photocatalytic NO oxidation activity of the pure $W_{18}O_{49}$ material in this case.

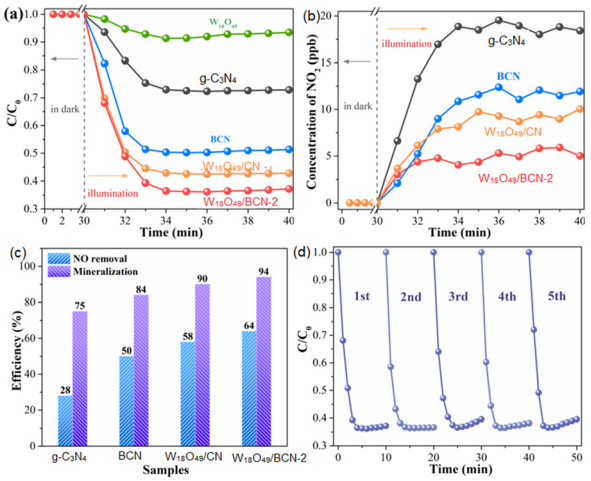

Fig. 6 (a) Photocatalytic NO removal plots of the samples under full spectrum conditions. (b) NO_2 (generated during NO oxidation) concentration plots of the samples. (c) NO removal and mineralization data of the samples. (d) NO removal cycling stability plots collected for the composite sample $W_{18}O_{49}$/BCN-2.

However, $W_{18}O_{49}$ nanobelt loaded BCN composites ($W_{18}O_{49}$/BCN samples) showed much-improved NO removal performance. Sample $W_{18}O_{49}$/BCN-2 attained the highest removal rate of 64% while sample $W_{18}O_{49}$/BCN-1 (having lower $W_{18}O_{49}$ loading than that of $W_{18}O_{49}$/BCN-2) and $W_{18}O_{49}$/BCN-3 (having higher $W_{18}O_{49}$ loading) revealed much lower NO removal efficiencies compared with that of sample $W_{18}O_{49}$/BCN-2, confirming that sample $W_{18}O_{49}$/BCN-2 has optimized $W_{18}O_{49}$ loading in this case. The performance was even higher than that of the commercial P25 material (TiO_2, attained a NO removal rate of 40%) and some of the literature reported materials.[17,18,23,24] The presence of B elements and the synergistic effects of the formed Z-scheme charge carrier transport system, as well as the LSPR effect and enhanced light absorption (owing to the incorporation of $W_{18}O_{49}$ nanocomponents) were beneficial for improving the photocatalytic NO oxidation efficiency of the $W_{18}O_{49}$/B-g-C_3N_4 composite material.

Since it is hard to have NO directly removed, it is often oxidized or reduced into other relatively easy-to-manage intermediate species before undergoing further reactions. The detailed photocatalytic NO oxidation processes with ·OH and $\cdot O_2^-$, the two major reactive radical species, are shown as follows.

$$W_{18}O_{49}/BCN + h\nu \rightarrow e^- + h^+ \quad (1)$$

$$e^- + O_2 \rightarrow \cdot O_2^- \quad (2)$$

$$NO + \cdot O_2^- \rightarrow NO_3^- \quad (3)$$

$$NO + \cdot O_2 \rightarrow NO_2 \quad (4)$$

$$\cdot O_2^- + H_2O + e^- \rightarrow H_2O_2 \quad (5)$$

$$\cdot O_2^- + H_2O_2 \rightarrow \cdot OH + OH^- \quad (6)$$

$$NO + \cdot OH \rightarrow HNO_2 \quad (7)$$

$$NO_2 + \cdot OH \rightarrow HNO_3 \quad (8)$$

NO in this case could be oxidized by the oxygen and $\cdot O_2^-$ radicals (generated from reactions between the photogenerated electrons and oxygen) to form NO_2 and NO_3^- intermediates. NO could also be oxidized into HNO_2 and HNO_3 species *via* further reactions with ·OH radicals that were generated from the H_2O_2 decomposition reaction.

Since the NO_2 species (generated as a by-product during NO oxidation reactions) is much more toxic than NO, it is important to attain full conversion of NO and monitor the concentration of NO_2 during the reaction. The utilization of catalysts with relatively low photocatalytic activity often results in incomplete oxidation of NO and high NO_2 by-product yield. Fig. 6b shows the NO_2 concentration *vs.* time curves obtained for the samples, with the $W_{18}O_{49}$/BCN-2 composite having the lowest NO_2 yield during the reaction. Moreover, sample $W_{18}O_{49}$/BCN-2 also showed the highest NO removal and mineralization efficiency, as observed in Fig. 6c, suggesting the tendency of NO in the reaction system to be converted into solid nitrate species instead of the NO_2 species. In addition, the cycling stability test results (Fig. 6d) confirmed that the similar level of reactivity has been retained after five cycles of measurements, indicating that the $W_{18}O_{49}$/BCN-2 composite catalyst has quite high stability in NO removal reactions.

To further examine the photocatalytic NO removal mechanisms, quantitative active species analysis was performed. NBT was used as the probe for $\cdot O_2^-$ radicals to determine the ability of the catalyst system in $\cdot O_2^-$ production by monitoring the changes in NBT absorption at 259 nm. As shown in Fig. 7a, the B doping and $W_{18}O_{49}$ loading in the $W_{18}O_{49}$/BCN-2 composites resulted in a significant decrease in absorption, indicating that a quite large amount of $\cdot O_2^-$ was generated. The $\cdot O_2^-$ yield data in Fig. 7b were estimated based on the stoichiometric ratio of NBT to $\cdot O_2^-$ being 1 : 1, and sample $W_{18}O_{49}$/BCN-2 showed the highest $\cdot O_2^-$ yield among all samples. For quantification of ·OH, terephthalate was used as the probe for ·OH radicals. In this case, since fluorescent dihydroxyterephthalic acid (2-HTA) could be obtained by the reaction between terephthalate and ·OH, by monitoring the changes in PL intensity of 2-THA at 425 nm, the ·OH generation ability of the catalyst samples could be determined, and the results are shown in Fig. 7c. The highest PL intensity observed for sample $W_{18}O_{49}$/BCN-2 was attributed to the narrow band gap, the extended light absorption range and the LSPR effect of the $W_{18}O_{49}$ material that allows the heterostructure system to generate ·OH and $\cdot O_2^-$ at the same time.

Quenching experiments were carried out to identify the active species using ESR measurements and to investigate the photocatalytic mechanisms. The ESR spin trapping test

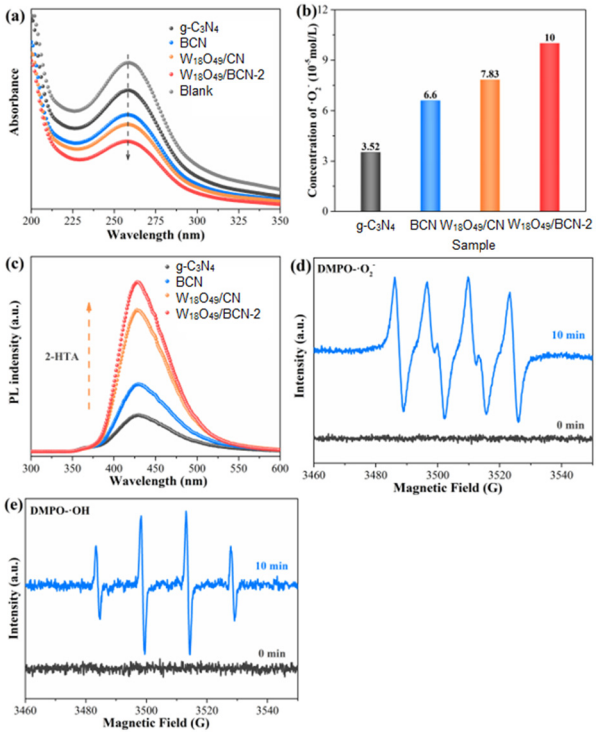

Fig. 7 (a) Absorption spectra of NBT containing sample suspension. (b) $\cdot O_2^-$ production data collected for the samples. (c) PL spectra of 2-HTA in different sample suspensions. (d and e) ESR spectra of the DMPO–$\cdot O_2^-$ and DMPO–·OH adducts in aqueous solution both in the dark and after light irradiation for the $W_{18}O_{49}$/BCN-2 catalyst system with the four DMPO–·OH peaks having an intensity ratio of 1 : 2 : 2 : 1.

data obtained on sample $W_{18}O_{49}$/BCN-2 are shown in Fig. 7d and e.

DMPO was utilized as the nitrone type spin trapping agent for monitoring the DMPO–radical adducts generated in methanol (for the DMPO–·OH adduct) and in water (for the DMPO–$\cdot O_2^-$ adduct). No adduct signal was observed for the samples tested in the dark. In contrast, both DMPO–$\cdot O_2^-$ and DMPO–·OH adduct signals were detected upon light irradiation, demonstrating that both $\cdot O_2^-$ and ·OH were the main active species generated in the $W_{18}O_{49}$/B-g-C_3N_4 composite catalytic system. In this case, the oxidation reactions occurred on the valence band of the B-g-C_3N_4 components owing to the ·OH/OH^- potential (2.59 eV), whereas the reduction reactions occurred on the $W_{18}O_{49}$ site due to the $O_2/\cdot O_2^-$ potential (−0.33 eV).

The schematic illustration of the $W_{18}O_{49}$/B-g-C_3N_4 heterostructure catalyst involving the proposed photocatalytic NO oxidation mechanism is shown in Scheme 2. Upon full spectrum light irradiation, transfer of photoexcited electrons occurred from the VB to the CB. Since a Z-scheme heterostructure composite was formed, the photogenerated electrons on the CB of the $W_{18}O_{49}$ components could combine with the holes at the VB of the BCN site, leading to accumulation of photoinduced holes at the VB of $W_{18}O_{49}$ and accumulation of electrons on the CB of BCN. These spatially separated electrons and holes could then migrate to the catalyst surface to initiate photocatalytic redox reactions. The immobilization of $W_{18}O_{49}$ and the constructed 2D/2D surface-to-surface structure with well-developed interfaces (as discussed above in the TEM section) significantly enhanced the separation efficiency of the photogenerated charge carriers of the $W_{18}O_{49}$/B-g-C_3N_4 composites. In addition, the introduced oxygen vacancies (due to $W_{18}O_{49}$ loading) in the heterostructure system were pivotal to enhancing the photocatalytic performance of the material. The LSPR of the $W_{18}O_{49}$ components (which was related to the collective oscillations of free charges originating from the lattice vacancies) could induce the generation of plasmonic hot electrons with high energy, causing continuous injection of hot electrons from the $W_{18}O_{49}$ site to the CB of BCN. The highly reactive $\cdot O_2^-$ radical species were generated by reactions between the activated O_2 (adsorbed onto the catalyst surface) and the photoinduced electrons as well as hot electrons, whereas ·OH radicals were generated by reactions between adsorbed H_2O and the photogenerated holes. In this case, most of the ·OH radicals were generated *via* H_2O oxidation with only a small proportion of ·OH generated *via* further $\cdot O_2^-$ reduction, and because of the presence of these highly reactive radicals ($\cdot O_2^-$ and ·OH), NO was preferably converted into solid nitrate species.

To further study the photocatalytic performance of the $W_{18}O_{49}$/B-g-C_3N_4 heterostructures, 4-NP reduction tests were

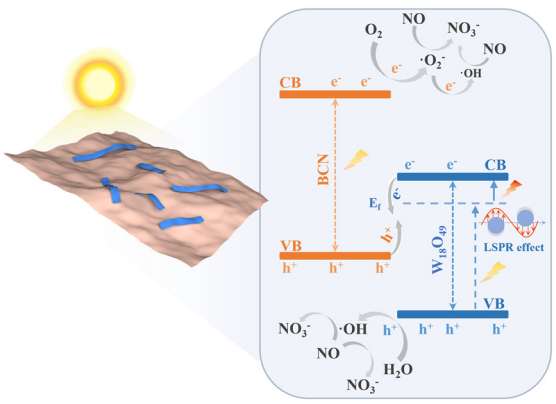

Scheme 2 Illustration of $W_{18}O_{49}$/B-g-C_3N_4 heterostructures involving photocatalytic processes.

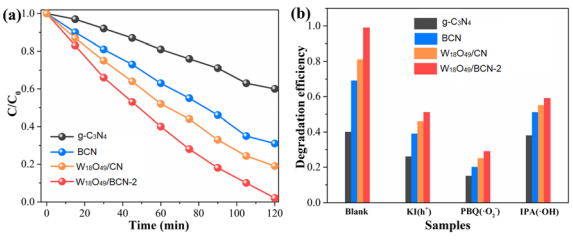

Fig. 8 (a) 4-NP reduction plot and (b) free radical trapping test results collected for the samples with the blank sample added for comparison.

carried out and the results are shown in Fig. 8a. In comparison with the pure g-C_3N_4 sample, the reduction efficiencies obtained for BCN, $W_{18}O_{49}$/CN and $W_{18}O_{49}$/BCN-2 samples were much higher. In this case, both B-doping and $W_{18}O_{49}$ immobilization improved the 4-NP reduction efficiency, and sample $W_{18}O_{49}$/BCN-2 revealed the highest performance attaining a high reduction rate of 99.9%. The free radical trapping test results in Fig. 8b showed that in the case of PBQ added as the scavenger for $\cdot O_2^-$, a drastic drop in 4-NP degradation rate was observed for all samples, indicating that $\cdot O_2^-$ served as the main active species during reduction reactions. When IPA as the ·OH trapping agent was added, a significant decrease in reduction rate was observed for sample $W_{18}O_{49}$/BCN-2, confirming that ·OH is another major active species in the reaction. In the case of KI addition (for capturing photogenerated holes), the photocatalytic performance of the samples was also decreased. Due to the quite high oxidative capacity of photogenerated holes, direct oxidation of 4-NP using these photoinduced holes could occur. However, in the case of $W_{18}O_{49}$/B-g-C_3N_4 heterojunctions, the Z-scheme charge transport paths allowed the much preferable oxidation of H_2O (using photoinduced holes) to generate more reactive ·OH species, attaining oxidation and degradation of 4-NP.

Conclusions

In summary, heterostructure formation, significantly suppressed charge carrier recombination, and enhanced solar light harvesting ability were the key factors that lead to the much-improved photocatalytic activity of the $W_{18}O_{49}$/B-g-C_3N_4 heterostructure catalysts. The combined treatments of the mechano-chemical pre-reaction and subsequent high-temperature multi-step thermal polymerization (for the fabrication of an ultrathin B-g-C_3N_4 base), as well as the solvothermal synthesis utilized for the horizontal implantation of $W_{18}O_{49}$ nanobelts on B-g-C_3N_4 were the keys for the formation of the $W_{18}O_{49}$/B-g-C_3N_4 Z-scheme heterostructure with extended light absorption (to the near infrared region) and improved interfacial structures. The 64% NO removal (higher than that of the commercial P25, with a quite low selectivity to NO_2 of 6.4%) and the 99% 4-NP reduction rate (to 4-aminophenol, under full-spectrum conditions) observed for the $W_{18}O_{49}$/B-g-C_3N_4 composites prepared using optimized parameters could be ascribed to the attained formation of the Z-scheme layered heterostructures possessing adjusted band structures, increased surface active sites and well-developed interfaces. These results offer paradigms for the development of efficient nanophotocatalysts for photocatalytic pollutant removal and environment-related applications.

Data availability

Data available on the request from authors.

Conflicts of interest

There are no conflicts to declare.

Acknowledgements

This work was supported in part by the National Natural Science Foundation of China, China (Grant no. 51972145), Ji Nan Science & Technology Bureau, China (Grant no. 2021GXRC109), and Science and Technology Program of University of Jinan, China (XKY2118).

Notes and references

1 X. Zhang, K. Matras-Postolek, P. Yang and S. P. Jiang, Cu Cluster Promoted Charge Separation and Transfer in Z-scheme WO_x/Cu-g-C_3N_4 heterojunctions towards efficient full solar-spectrum photocatalysis, *J. Colloid Interface Sci.*, 2023, **636**, 646–656.
2 F. Pellegrino, L. Pellutiè, F. Sordello, C. Minero, E. Ortel, V. Hodoroaba and V. Maurino, Influence of agglomeration and aggregation on the photocatalytic activity of TiO_2 nanoparticles, *Appl. Catal., B*, 2017, **216**, 80–87.
3 F. Gholami, M. Tomas, Z. Gholami and M. Vakili, Technologies for the nitrogen oxides reduction from flue gas: A review, *Sci. Total Environ.*, 2020, **714**, 136712.
4 H. Zhang, X. Zhang, C. Xie, W. Shi and P. Yang, TiO_2 Nanocrystals Decorated Superior Thin $Ti_3C_2T_x$ Nanosheets towards Efficient NO Removal, *Environ. Res.*, 2023, **227**, 115793.
5 Y. Inomata, H. Kubota, S. Hata, E. Kiyonaga, K. Morita, K. Yoshida, N. Sakaguchi, T. Toyao, K. Shimizu, S. Ishikawa, W. Ueda, M. Haruta and T. Murayama, Bulk tungsten-substituted vanadium oxide for low-temperature NOx removal in the presence of water, *Nat. Commun.*, 2021, **12**, 557.
6 H. Zhang, B. Xu, X. Zhang and P. Yang, Raspberry-like TiO_2 hollow spheres consisted of small nanocrystals towards efficient NO removal, *Environ. Sci.: Nano*, 2022, **9**, 3397–3406.
7 Z. Jiang, X. Zhang, H. S. Chen, P. Yang and S. P. Jiang, Fusiform g-C_3N_4 capsules with superior photocatalytic activity, *Small*, 2020, **16**, 2003910.
8 X. Zhang, P. Yang, H. S. Chen and S. P. Jiang, Carbon Layer Derived Carrier Transport in Co/g-C_3N_4 Nanosheet Junctions for Efficient H_2O_2 Production and NO Removal, *Chem. Eng. J.*, 2024, **479**, 147609.
9 X. Zhang and P. Yang, Role of Graphic Carbon in g-C_3N_4 Nanoarchitectonics towards Efficient Photocatalytic Reaction Kinetics: A Review, *Carbon*, 2024, **216**, 118584.
10 T. Song, X. Zhang, K. Matras-Postolek and P. Yang, N-doped carbon layer promoted charge separation/transfer in WP/g-C_3N_4 heterostructures for efficient H_2 evolution and 4-NP removal, *Carbon*, 2023, **202**, 378–388.
11 X. Zhang and S. P. Jiang, Layered TiO_2/g-C_3N_4 nanocomposites for efficient photocatalytic water splitting

and CO_2 reduction: A review, *Mater. Today Energy*, 2022, **23**, 100904.
12 Y. Tseng and C. Kuo, Photocatalytic degradation of dye and NOx using visible-light-responsive carbon-containing TiO_2, *Catal. Today*, 2011, **174**, 114–120.
13 P. X. Zhao, X. W. Feng, D. S. Huang, G. Y. Yang and D. Astruc, Basic concepts and recent advances in nitrophenol reduction by gold- and other transition metal nanoparticles, *Coord. Chem. Rev.*, 2015, **287**, 114–136.
14 X. Zhang, K. Zhu, C. Xie and P. Yang, Vertically implanting $MoSe_2$ nanosheets on superior thin C-doped g-C_3N_4 nanosheets towards interface-enhanced electrochemical activities, *Carbon*, 2024, **220**, 118884.
15 S. Tong, X. Zhang and P. Yang, g-C_3N_4 sheet nanoarchitectonics with island-like crystalline/amorphous homojunctions towards efficient H_2 and H_2O_2 evolution, *Environ. Res.*, 2023, **236**, 116805.
16 L. Duan, G. Li, S. Zhang, H. Wang, Y. Zhao and Y. Zhang, Preparation of S-doped g-C_3N_4 with C vacancies using the desulfurized waste liquid extracting salt and its application for NO_x removal, *Chem. Eng. J.*, 2021, **411**, 128551.
17 T. Song, X. Zhang, K. Matras-Postolek and P. Yang, Cobalt clusters in superior thin g-C_3N_4 nanosheets for enhanced H_2/H_2O_2 generation and NO removal, *J. Environ. Chem. Eng.*, 2022, **10**, 108747.
18 G. Dia, Z. Zhu, H. Zhang, Y. g. Qiu, D. Yin and J. Crittenden, Simultaneous sulfamethazine oxidation and bromate reduction by Pd mediated Z-scheme Bi_2MoO_6/g-C_3N_4 photocatalysts: Synergetic mechanism and degradative pathway, *Chem. Eng. J.*, 2020, **402**, 126061.
19 X. Zhang, X. R. Zhang, P. Yang and S. P. Jiang, Transition metals decorated g-C_3N_4/N-doped carbon nanotube catalysts for water splitting: a review, *J. Electroanal. Chem.*, 2021, **895**, 115510.
20 X. Zhang, P. Yang and S. P. Jiang, NiCo-layered double hydroxide/g-C_3N_4 heterostructures with enhanced adsorption capacity and photo reduction of Cr(VI), *Appl. Surf. Sci.*, 2021, **556**, 149772.
21 X. Xua, Y. Huang, K. Daia, Z. Wang and J. Zhang, Non-noble-metal CuSe promotes charge separation and photocatalytic CO_2 reduction on porous g-C_3N_4 nanosheets, *Sep. Purif. Technol.*, 2023, **317**, 123887.
22 K. Ariga, Nanoarchitectonics: the method for everything in materials science, *Bull. Chem. Soc. Jpn.*, 2024, **97**, uoad001.
23 T. Paik, M. Cargnello, T. R. Gordon, S. Zhang, H. Yun, J. D. Lee, H. Y. Woo, S. J. Oh, C. R. Kagan, P. Fornasiero and C. B. Murray, Photocatalytic Hydrogen Evolution from Substoichiometric Colloidal WO_{3-x} Nanowires, *ACS Energy Lett.*, 2018, **3**, 1904–1910.
24 I. M. Szilágyi, B. Fórizs, O. Rosseler, Á. Szegedi, P. Németh, P. Király, G. Tárkányi, B. Vajna, K. Varga-Josepovits and K. László, WO_3 photocatalysts: Influence of structure and composition, *J. Catal.*, 2012, **294**, 119–127.
25 K. Deng, Z. Hou, X. Deng, P. Yang, C. Li and J. Lin, Enhanced Antitumor Efficacy by 808 nm Laser-Induced Synergistic Photothermal and Photodynamic Therapy Based on a Indocyanine-Green-Attached $W_{18}O_{49}$ Nanostructure, *Adv. Funct. Mater.*, 2015, **25**, 7280–7290.
26 H. B. Truong, B. T. Huy, S. K. Ray, Y. I. Lee, J. Cho and J. Hur, H_2O_2-assisted photocatalysis for removal of natural organic matter using nanosheet C_3N_4-WO_3 composite under visible light and the hybrid system with ultrafiltration, *Chem. Eng. J.*, 2020, **399**, 125733.
27 C. Jia, X. Zhang, K. Matras-Postolek, B. Huang and P. Yang, Z-scheme rGO/TiO_2-bronze/$W_{18}O_{49}$ ternary heterostructure towards efficient full solar-spectrum photocatalysis, *Carbon*, 2018, **139**, 415–426.
28 B. Chai, C. Liu, J. Yan, Z. Ren and Z. Wang, In-situ synthesis of WO_3 nanoplates anchored on g-C_3N_4 Z-scheme photocatalysts for significantly enhanced photocatalytic activity, *Appl. Surf. Sci.*, 2018, **448**, 1–8.
29 X. Zhang, K. Matras-Postholes, P. Yang and S. P. Jiang, Pt clusters in carbon network to enhance photocatalytic CO_2 and benzene conversion of WO_x/g-C_3N_4 nanosheets, *Carbon*, 2023, **214**, 118337.
30 T. Song, X. Zhang, Q. Che and P. Yang, Heterojunction nanoarchitectonics with SnS_2/g-C_3N_4 S-scheme toward enhanced photooxidation and photoreduction, *J. Ind. Eng. Chem.*, 2022, **113**, 389–400.
31 X. Zhang, X. R. Zhang, P. Yang, H.-S. Chen and S. P. Jiang, Black Magnetic Cu-g-C_3N_4 Nanosheets for Efficiently Photocatalytic H_2 generation and CO_2/Benzene Conversion, *Chem. Eng. J.*, 2022, **450**, 138030.
32 X. Zhang, K. Matras-Postolek and P. Yang, Heterojunction Nanoarchitectonics of WO_x/Au-g-C_3N_4 with Efficient Photogenerated Carrier Separation and Transfer toward Improved NO and Benzene Conversion, *Mater. Today Adv.*, 2023, **17**, 100355.
33 X. Zhang, J.-P. Veder, S. i. He and S. P. Jiang, Construction of 2D g-C_3N_4 lateral-like homostructures and their photo- and electro-catalytic activities, *Chem. Commun.*, 2019, **55**, 1233–1236.
34 X. Zhang, P. Yang and S. P. Jiang, Edge-epitaxial growth of layered yellow g-C_3N_4 on red g-C_3N_4 nanosheets and their superior photocatalytic activities, *Chem. Commun.*, 2021, **57**, 3119–3122.
35 K. Deng, Z. Hou, X. Deng, P. Yang, C. Li and J. Lin, Enhanced Antitumor Efficacy by 808 nm Laser-Induced Synergistic Photothermal and Photodynamic Therapy Based on a Indocyanine-Green-Attached $W_{18}O_{49}$ Nanostructure, *Adv. Funct. Mater.*, 2015, **25**, 7280–7290.
36 R. Hailili, H. W. Ji, K. W. Wang, X. A. Dong, C. C. Chen, H. Sheng, D. W. Bahnemann and J. C. Zhao, ZnO with Controllable Oxygen Vacancies for Photocatalytic Nitrogen Oxide Removal, *ACS Catal.*, 2022, **12**, 10004–10017.